



# Effect of microsegregation and heat treatment on localised $\gamma$ and $\gamma'$ compositions in single crystal Ni-based superalloys

V.C.I. Strutt <sup>a,\*</sup>, B.M. Jenkins <sup>a</sup>, J.M. Woolrich <sup>b</sup>, M. Appleton <sup>b</sup>, M.P. Moody <sup>a</sup>, P.A.J. Bagot <sup>a</sup>

<sup>a</sup> Department of Materials, University of Oxford, Oxford OX1 3PH, UK

<sup>b</sup> Rolls-Royce plc, PO Box 31, Derby DE24 8BJ, UK

## ARTICLE INFO

### Article history:

Received 26 January 2023

Received in revised form 24 March 2023

Accepted 27 March 2023

Available online 28 March 2023

### Keywords:

Characterization

Atom probe tomography

Micro-segregation

Ni-base single crystal superalloys

Interfacial behaviour

## ABSTRACT

The present work investigates the impact of residual segregation on the underlying microstructure of a 3rd generation single crystal, nickel-based superalloy to understand potential variation in mechanical behaviour between dendrite cores and interdendritic regions. Despite the applied heat-treatments, chemical variation between dendrite cores and interdendritic regions persisted particularly for elements Re, Nb and Ta. Atom probe tomography (APT) was utilized for its nanoscale capability to map site-specific chemical changes in the  $\gamma$  matrix,  $\gamma'$  precipitates and across the  $\gamma/\gamma'$  interface. Greater interfacial segregation of Re, matched by a corresponding depletion of Ni were observed within dendrite cores, with the extent found to increase following heat treatment. Differences in lattice parameters between dendrite cores and interdendritic regions were identified, with larger lattice misfits associated with interdendritic regions.

© 2023 The Authors. Published by Elsevier B.V. This is an open access article under the CC BY license (<http://creativecommons.org/licenses/by/4.0/>).

## 1. Introduction

Single crystal nickel-based superalloys have excellent high temperature capabilities largely derived from their highly coherent two-phase microstructures.  $\text{Ni}_3\text{Al}$  gamma prime ( $\gamma'$ ) precipitates with an  $\text{L}_{12}$  crystal structure, accounting for roughly 70% volume fraction in currently used alloys, reside within a face-centred cubic (FCC) gamma ( $\gamma$ ) matrix. A low homologous temperature and the preservation of mechanical properties at elevated operating temperatures makes them the material of choice for high temperature turbine blade applications [1]. Solid solution and precipitate strengthening are the predominant strengthening mechanisms, with both effects achieved through selective alloying additions and heat treatments. Re, Co and W promote solid solution strengthening by distorting local lattices and inhibiting dislocation motion, whilst Al, Ti and Ta augment the formation of  $\gamma'$  precipitates, which similarly impede dislocation motion through the lattice [2]. Composition, distribution, volume fraction ( $V_f$ ) and interfacial behaviour of  $\gamma'$  precipitates all play important roles in the degree of alloy strengthening [3–6].

Whilst alloying additions are essential in achieving the desired microstructure and subsequent mechanical properties, differences in solubility and kinetic behaviour between elements can lead to severe microsegregation during casting [7–9]. Despite post-

solidification heat treatments designed to homogenise the alloy, a degree of segregation persists leading to chemical heterogeneity between the dendrites and interdendritic regions, which cannot be fully eliminated due to the impractical treatment times and costs required [10]. Previous studies employing EDX and EPMA have convincingly shown Re, Co and W segregating into the dendrite cores (DCs) and Al, Ti and Ta enriching interdendritic regions (IDRs), with the partitioning extent decreasing with progressively longer and hotter heat treatments [11–13]. Although element partitioning behaviour has been extensively mapped on the micrometre scale between DCs and IDRs, to date, fewer studies have attempted to measure the extent of segregation on the nanoscale and its subsequent effects on the local compositions of  $\gamma$  and  $\gamma'$ . Differences in mechanical responses between the DCs and IDRs have been reported with conflicting conclusions. One study observed definite increases in hardness associated with DCs [14], where more refractory elements had segregated in a fourth generation Ni-superalloy, whilst another found IDRs displayed a higher hardness which was attributed to a larger  $V_f$  of the strengthening  $\gamma'$  phase [15].

Along with solute partitioning ahead of the liquid-solid interface causing compositional variations in dendrites, solute partitioning also occurs between the  $\gamma$  and  $\gamma'$  phases. First principle calculations coupled with experimental data have shown Co, Cr, Mo, W and Re enrich within the  $\gamma$  phase whilst Ti, Ta, Nb and Al enrich within  $\gamma'$  precipitates [16–18]. Accurately measuring the composition of  $\gamma$  and  $\gamma'$  is difficult due to the small  $\gamma'$  precipitate size and often even

\* Corresponding author.

E-mail address: [victoria.strutt@materials.ox.ac.uk](mailto:victoria.strutt@materials.ox.ac.uk) (V.C.I. Strutt).

narrower widths of channels of  $\gamma$  matrix between such finely-packed precipitates.

The  $\gamma/\gamma'$  interface plays a pivotal role in determining the microstructure and mechanical properties of these two-phase alloys, but the nanoscale nature of this interface makes it challenging to characterise its composition. Multiple studies have focused in particular on understanding the role of Re, which is believed to be an essential element in stabilizing the interface and influencing the mechanical properties of various alloys [19–22]. Due to its enhanced spatial and chemical resolution, atom probe tomography (APT) has been increasingly utilised to characterize  $\gamma$  and  $\gamma'$  compositions and  $\gamma/\gamma'$  interfaces within Ni-based superalloys [16,23–26]. Interfacial segregation of Re and Co with corresponding depletions of Ni at the  $\gamma/\gamma'$  interface have been reported in studies using APT [23,27]. However, neither nanoscale investigations nor those on larger scales have compared differences in  $\gamma/\gamma'$  interface between those occurring within DCs and IDRs, respectively.

Many of the prior studies employing APT to investigate Ni-superalloys use electropolishing specimen preparation methods. Although more convenient, electropolishing samples random, non-site specific regions within the microstructure [28]. Sampling random regions in this manner disregards any variation in sample composition from microsegregation. Neglecting possible discrepancies in composition between DCs and IDRs will affect all compositional APT data extracted, due to the sampling volume limitations of the technique. More site-specific studies are therefore needed correlating compositional changes driven through microsegregation with changes observed in local  $\gamma$  and  $\gamma'$  compositions, morphology, and interfacial behaviour. Combining high-resolution APT with larger-scale complementary techniques will allow for a thorough characterisation of Ni-superalloys across different length scales. This information could help inform observations about mechanical property variations observed between DCs and IDRs, inform better heat-treatment processes and help ensure alloy stability in future components.

This study compares the compositions of DCs and IDRs in as-cast and heat-treated samples of a 3rd generation Ni-based superalloy. We observe differences in composition between DCs and IDRs which translate to differences in  $\gamma$  and  $\gamma'$  compositions within these two regions. In addition, variations in interfacial segregation,  $\gamma'$  morphology and volume fraction are also observed. Properly understanding these variations is important, as they may all have significant consequences for the mechanical properties and corrosion behaviour of these alloys during service.

## 2. Materials and methods

Bars of directionally solidified Ni-based single-crystal superalloy RR3010, with a nominal composition of 13.7Al-1.9Cr-3.3Co-0.3Mo-3.0Ta-1.9W-0.1Ti-2.3Re-0.03Nb-BaI.Ni (at%) were provided by Rolls Royce plc. One set of samples was left in the as-cast condition, whilst the rest were subjected to an initial solution heat treatment before precipitation and aging treatments at approximately 1200 °C and 900 °C respectively. Regardless of the treatment history, 3 mm disc samples were then cut perpendicular to the [001] direction and metallographically prepared to a finish of 0.04  $\mu\text{m}$  colloidal silica.

Qualitative microanalysis of dendrite formation was performed using a Zeiss EVO scanning electron microscope (SEM) fitted with an Oxford Instruments X-act energy dispersive x-ray spectrometer (EDX). Backscattered electron (BSE) images were used to identify dendritic regions within the microstructure and micro-compositional information was collected using EDX at an accelerating voltage of 20 kV. Compositional analysis was collected from 10 dendrite cores and 10 interdendritic regions. APT samples were taken from several dendrite cores and interdendritic regions identified within each sample, prepared via a conventional focussed ion beam (FIB)

lift-out method using a Zeiss Nvision 40 SEM-FIB [29]. Atom probe analysis was performed in laser-mode with a laser energy of 50 pJ, at 50 K with a detection rate of 0.005 atoms per pulse on a LEAP 5000 XR at the University of Oxford. CAMECA APSUITE 6.1 software was used to reconstruct and analyse the collected data, with peak overlap deconvolution performed using by the method described by London [30].

## 3. Results

### 3.1. As-received RR3010

#### 3.1.1. S As-received microstructure and dendritic segregation

SEM micrographs of the as-cast alloy imaged using backscattered electrons displayed large-scale dendrite formation across the entire sample surface, where dendrites formed large, lobed features surrounded by IDRs (Fig. 1a). Most individual dendrites in the as-cast condition contained brighter central regions within the dendrites, denoted as DCs, with more diffuse peripheral lobes suggesting compositional variations are present even within the dendrites (Fig. 1a). The inter-dendrite spacing was measured from core to core between neighbouring dendrites, with 10 individual dendrites chosen such that no dendrites shared neighbours. The spacing measured in this way was found to be  $189 \pm 22 \mu\text{m}$ .

Fig. 1b shows an interdendritic region surrounded by three dendrite lobes highlighting the change in  $\gamma'$  morphology between dendrites and interdendritic regions. This change can be further observed in more detail in Fig. 1c–e, where the various regions have been magnified. Smaller  $\gamma'$  precipitates within dendrites were observed with a bigger distribution of sizes and larger  $\gamma$  channels, the latter indicative of a lower  $\gamma' V_f$  (Fig. 1c). In contrast,  $\gamma'$  within IDRs fell into two distinct morphologies;  $\gamma'$  precipitates forming elongated cellular structures (Fig. 1d) and finer  $\gamma'$  precipitates surrounded by narrow  $\gamma$  channels (Fig. 1e). EDX performed on the as-cast samples showed clear segregation of elements, with Re and W segregating into DCs whilst Al and Ta segregated into IDRs (Fig. 1f). Other elements also displayed a degree of segregation into DCs or IDRs, but this was less qualitatively clear from the EDX maps.

To quantitatively assess element partitioning into the DCs and IDRs, the partitioning coefficient  $K_i^{DC/IDR} = C_i^{DC}/C_i^{IDR}$  is used, where  $C_i^{DC}$  is the concentration of element  $i$  in DCs and  $C_i^{IDR}$  is the concentration of element  $i$  in IDRs. The partitioning coefficient results, summarised in Table 1, unambiguously demonstrate that, in as-cast samples, Re, Co, W and Cr partition into DCs while Al and Ta partition into IDRs. Ni  $K_i^{DC/IDR}$  values remain roughly at unity suggesting no segregation preference. The values in the heat-treated samples are discussed separately in Section 3.2.

#### 3.1.2. Atomic-scale phase analysis

To understand how the noted compositional variations between DCs and IDRs affected the local compositions and morphologies of  $\gamma$  and  $\gamma'$ , APT analysis was performed on individual DCs and IDRs. As-cast sample atom maps, shown in Fig. 2, taken from a DC (Fig. 2a) and IDR (Fig. 2b), respectively, clearly show the distinct  $\gamma$  and  $\gamma'$  phases as demarcated by Al, Ni and Ta ( $\gamma'$  phases) and Cr, Co and Re ( $\gamma$  matrix). As-cast specimens taken from DCs show blocky, irregularly-shaped  $\gamma'$  precipitates with a larger distribution of sizes compared to IDRs, where  $\gamma'$  precipitates were more regular in both shape and size. Fewer APT experiments captured  $\gamma$  matrix channels in the IDRs, suggesting larger  $\gamma'$  precipitates and with a higher  $V_f$ . Both observations correlate with the SEM results (Fig. 1c–e), where distinct differences in  $\gamma'$  morphology were clearly observed between DCs and IDRs.

To obtain phase compositions,  $\gamma$  and  $\gamma'$  phases were separated by applying an Al isoconcentration surface which resulted in the

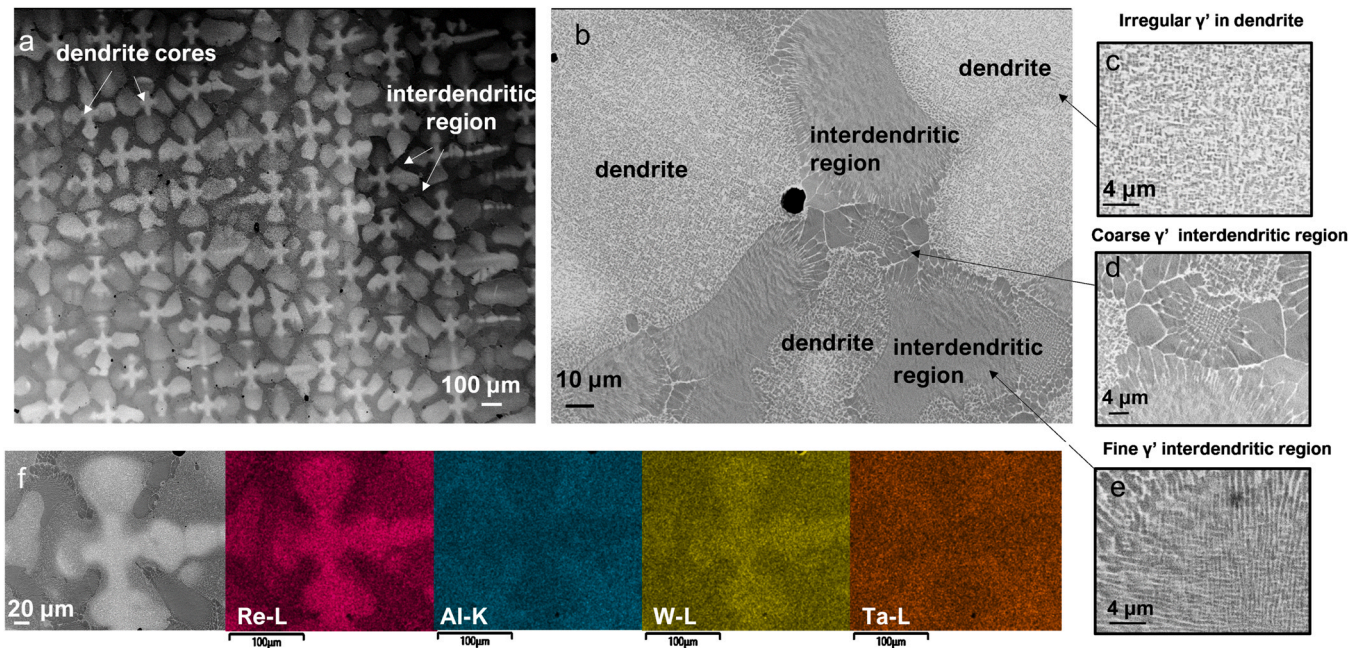


**Fig. 1.** Backscattered electron images showing (a) cross sectional microstructure of as-cast single crystal RR3010 showing prolific dendrite formation (b) magnified IDRs surrounded by dendrites displaying morphology variation in  $\gamma'$  precipitates with magnified regions (c-e). (f) backscatter electron image and corresponding element distribution maps of Re, Al, W and Ta within dendrites and interdendritic region.

**Table 1**

Partitioning coefficient of elements into DCs and IDRs as measured by EDX (\*estimation as concentration is approaching detection limit of EDX detector).

	at%	Ni	Re	W	Al	Co	Mo	Ta	Ti*	Nb*	Cr
EDX	As cast $K_i^{DC/IDR}$	$1.0 \pm 0.1$	$2.4 \pm 0.2$	$1.9 \pm 0.2$	$0.8 \pm 0.1$	$1.3 \pm 0.4$	$0.7 \pm 0.3$	$0.2 \pm 0.1$	$1.3 \pm 0.9$	$1.3 \pm 0.9$	$2.0 \pm 0.3$
	Heat Treated $K_i^{DC/IDR}$	$1.00 \pm 0.1$	$1.8 \pm 0.2$	$1.1 \pm 0.1$	$0.9 \pm 0.2$	$1.0 \pm 0.2$	$0.8 \pm 0.3$	$0.9 \pm 0.1$	$1.5 \pm 1.0$	$1.1 \pm 0.8$	$1.4 \pm 0.2$

narrowest interfacial width with respect to Al, as defined in the method in Homer et al. [31]. Compositions were obtained from an atom-count weighted average of three regions of interest within each phase. These results are presented in the bar graphs in Fig. 2c.

Using phase compositions, the partitioning of elements into  $\gamma$  and  $\gamma'$  was calculated using a similar equation:  $K_i^{\gamma/\gamma'} = C_i^{\gamma}/C_i^{\gamma'}$  where  $C_i^{\gamma'}$  is the concentration of element  $i$  in  $\gamma'$  and  $C_i^{\gamma}$  is the concentration of element  $i$ . Fig. 3 demonstrates that Re, Mo, Cr, Co and W partition into the  $\gamma$  matrix, with Re displaying the strongest degree of partitioning, whilst Ta, Nb, Ti, Al and Ni partition into the  $\gamma'$ . The partitioning extent of each element correlated with microscopic region; a higher degree of partitioning was observed for  $\gamma$  forming elements within DCs, where these elements had enriched (according to EDX). Similarly,  $\gamma'$  forming elements partitioned more strongly into the  $\gamma'$  phase within IDRs.

### 3.2. Heat-treated RR3010

#### 3.2.1. Microstructural changes in heat-treated RR3010

SEM micrographs (using backscattered electrons) on heat-treated samples again displayed contrast variation, suggesting residual segregation remained after solutionizing and primary aging. However, distinct dendrite shapes were no longer visible (Fig. 4a). Previous dendrite outlines appeared to have partially dissolved, with dendrites now interconnected. Several isolated pools were observed within IDRs, believed to be residual eutectic. This dissolution of dendrites was confirmed qualitatively by EDX, where only Re displayed mild segregation to DCs while Al and Ta enriched into the isolated eutectic pools (Fig. 4f). The morphology and size

distribution of  $\gamma'$  precipitates were now more consistent across IDRs and DCs, as seen in magnified regions of the microstructure in Fig. 4d-e. The exception was the isolated IDRs eutectic pools (Fig. 4c), where  $\gamma'$  exclusively formed large, elongated precipitates. Core-to-core inter-dendrite distances remained largely unchanged after heat treatment at  $164 \pm 28 \mu\text{m}$ . Compositions of DCs and IDRs were measured in heat-treated samples and used to estimate the extent of partitioning between the two regions as previously done for as-cast samples, which is also shown in Table 1. Whilst the heat treatment caused  $K_i^{DC/IDR}$  values to approach unity, indicating homogenisation, partial segregation remains for many elements in the alloy.

#### 3.2.2. Evolution of phase chemistry after heat treatment

Specific samples from DCs and IDRs were once again examined by APT to understand effects of microsegregation on local  $\gamma$  and  $\gamma'$  compositions. From the atom maps shown in Fig. 5, it is evident that the heat treatment has caused morphological differences; whilst blocky, irregular  $\gamma'$  precipitates within the dendrite core were observed in as-cast samples (Fig. 2a), the heat-treated specimens show near straight, regular-sided  $\gamma'$  precipitates (Fig. 5a). Whilst it is impossible to capture an entire  $\gamma'$  precipitate within the analysis volume of an atom probe experiment due to the sampling size limitations, this shift suggests a transition from irregular to cuboidal  $\gamma'$  precipitation. This morphological transformation can also be seen using SEM by comparing the backscattered magnified images of DCs before (Fig. 1c) and after heat treatment (Fig. 4e). A transition was less obvious in the atom maps from IDRs, where  $\gamma'$  morphologies appeared unchanged following heat treatment, however a higher proportion of gamma channels were observed within atom probe analysis volumes of heat-treated IDR samples, suggesting a



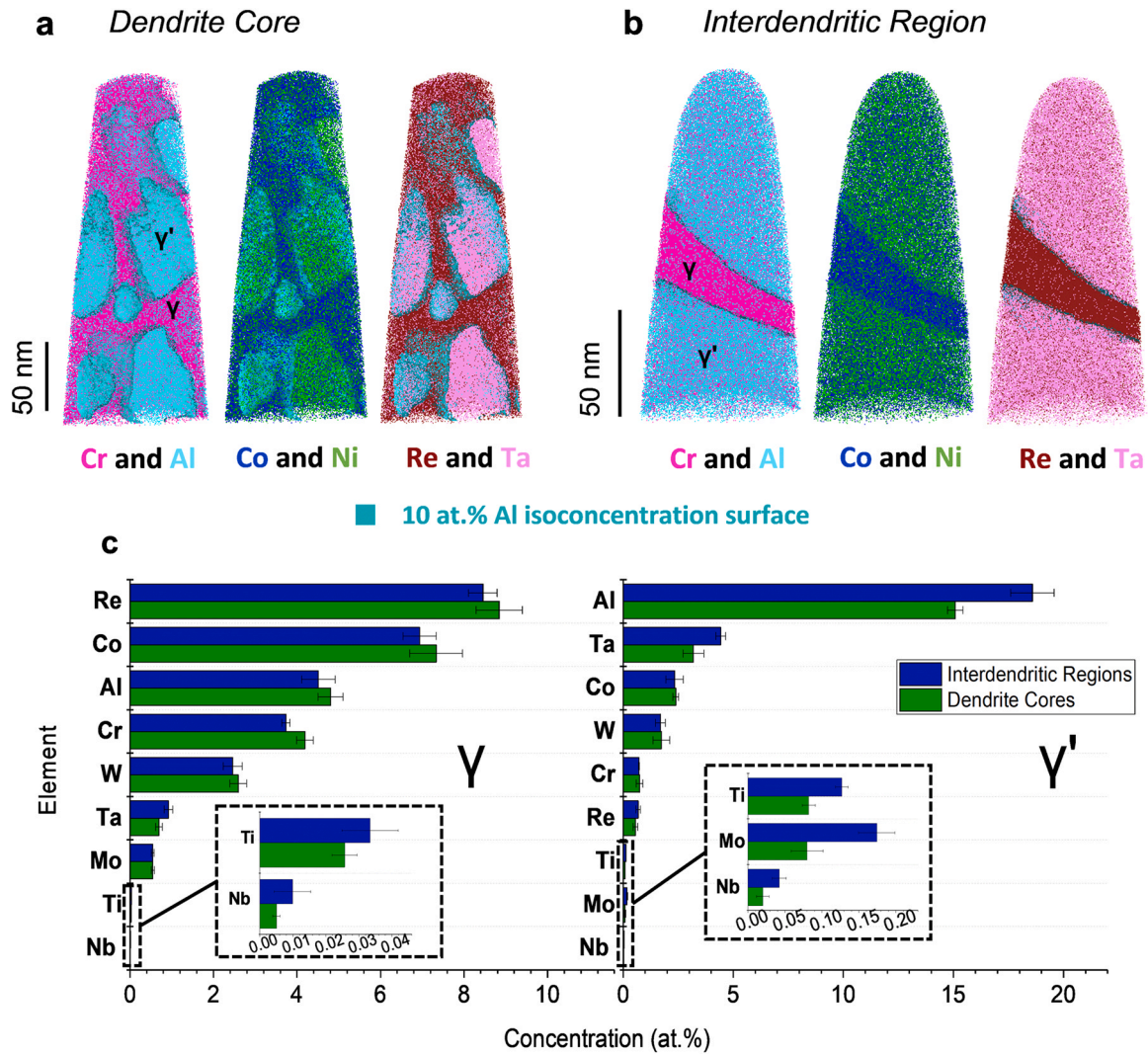


**Fig. 2.** Atom maps from as-cast RR3010 samples showing Cr, Al, Co, Ni, Re and Ta atoms in (a) dendrite cores and (b) interdendritic regions. (c) composition of  $\gamma$  and  $\gamma'$  phases in as-cast samples as determined by APT.

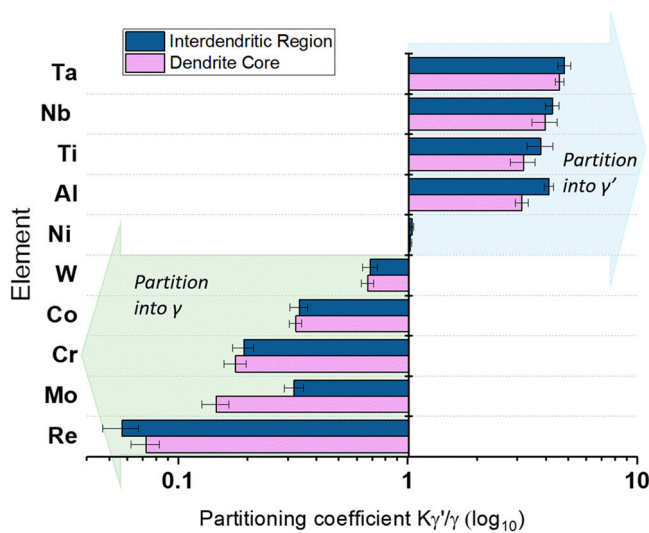


**Fig. 3.** Partitioning ratio of elements into  $\gamma$  and  $\gamma'$  within dendrite cores and interdendritic regions in as-cast RR3010 samples.

qualitative reduction in  $V_f$  of  $\gamma'$  precipitates. This reduction in  $V_f$  was supported by lever rule plots and further discussed in Section 3.3.

Phase compositions were also measured in the heat-treated samples, where it was noted that the composition of  $\gamma'$  precipitates between DCs and IDRs were more consistent. This was also true for  $\gamma$  phases, with results shown in the bar graphs of Fig. 5c. Despite the DCs and IDRs becoming more uniform in composition after heat treatment, a measurable difference in composition remains. This correlated with the EDX data, most apparently for Re, Co and Al. Whilst the absolute difference in element concentration might appear small between DCs and IDRs, Fig. 5c, this results in a large relative change when considering the total concentration of each element present in each phase.

The partitioning preference for elements to reside in the  $\gamma$  or  $\gamma'$  phases for  $\gamma$  forming elements remained largely unchanged after heat treatment, with Re still partitioning the strongest into  $\gamma$  followed by Cr, Co, Mo and W (Fig. 6). However, after heat treatment there was a large increase in the extent of Ti and Al partitioning into the  $\gamma'$  compared to the other  $\gamma'$  forming elements with Ti  $K_{\gamma'/\gamma}$  increasing by 1.4 and 1.1 in the DCs and IDRs respectively and Al  $K_{\gamma'/\gamma}$  increasing by 1.4 and 0.9 in the DCs and IDRs respectively. This suggests the heat treatment more strongly drives Ti and Al into the  $\gamma'$



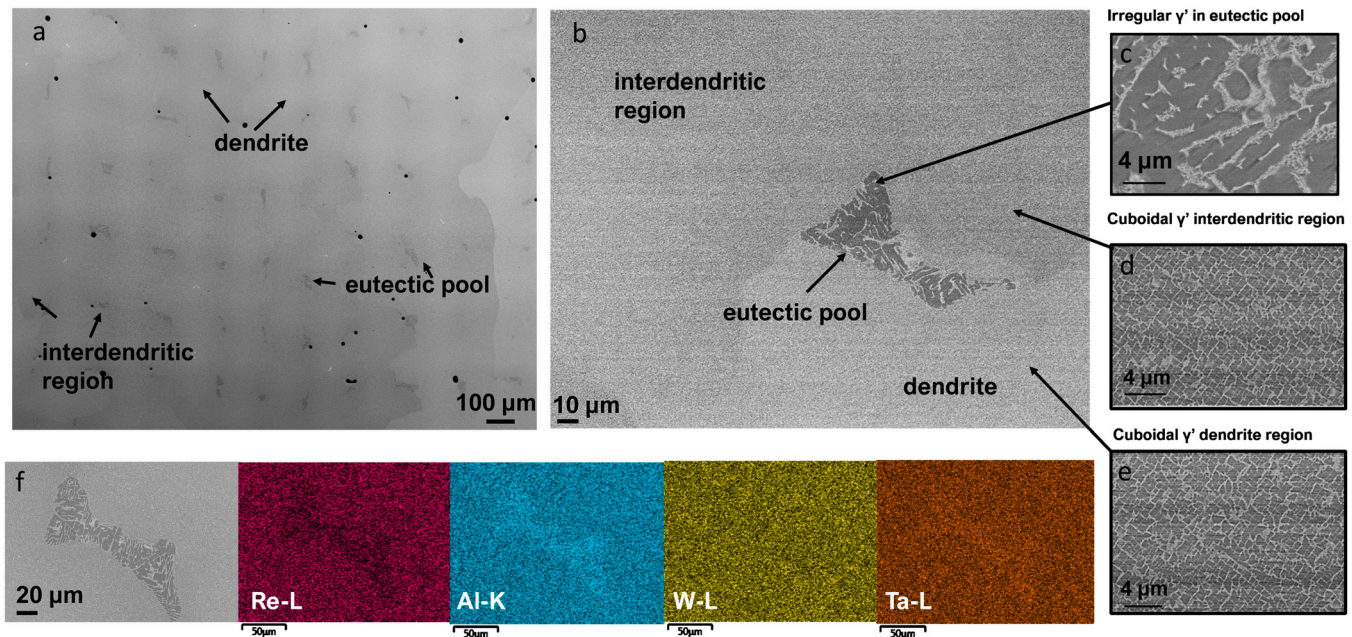


**Fig. 4.** Backscattered electron images showing (a) cross sectional microstructure of heat-treated single crystal RR3010 reduced dendrite formation, (b) magnified IDRs surrounded by dendrites displaying morphology variation in  $\gamma'$  precipitates with magnified regions (c-e). (f) backscatter electron image and corresponding element distribution maps of Re, Al, W and Ta within dendrites and interdendritic region.

precipitates. Aside from Cr and Re in IDRs, all elements partitioned more strongly after the heat treatment into their respective preferred phases. In addition to the large  $\gamma'$  precipitates observed, smaller spheroidal secondary  $\gamma'$  precipitates < 10 nm in diameter were visible within wider  $\gamma$  channels in samples from both IDRs and DCs (as visible for DCs in Fig. 5a).

### 3.3. Volume fraction, $V_f$

The measured compositions of individual phases can be used to estimate  $V_f$  of  $\gamma'$  by employing the lever rule:  $C_n = V_f C_{\gamma'} + (1 - V_f) C_\gamma$  where  $C_n$ ,  $C_{\gamma'}$  and  $C_\gamma$  are the concentrations of the bulk alloy,  $\gamma'$  and  $\gamma$  phases respectively.  $C_n$  is calculated from the contributions of all equivalent datasets from within one region. Therefore, it must be noted that  $V_f$  calculations assume that the correct phase fractions have been sampled within each region.  $V_f$  can thus be found from the gradient of a straight-line plot of  $C_n - C_\gamma$  against  $C_{\gamma'} - C_\gamma$  plotted for each respective element as demonstrated in Fig. 7. Table 2 shows the calculations of  $V_f$  for the different conditions and regions. In the as-cast conditions IDRs display much higher  $V_f$  compared to DCs but after heat treatment the calculated  $V_f$  values appear more homogenised across both regions, with only a small disparity between  $V_f$  measured for DCs and IDRs where the increase in  $V_f$  of IDRs compared to DCs was within estimated errors of this calculation. Note that (smaller) secondary  $\gamma'$  precipitates were not included in  $V_f$  calculations to enable direct comparison with estimates from lower spatial resolution techniques. However, the size of the secondary  $\gamma'$  precipitates in comparison to the large  $\gamma'$  phase means they are unlikely to make a significant difference to the obtained values.

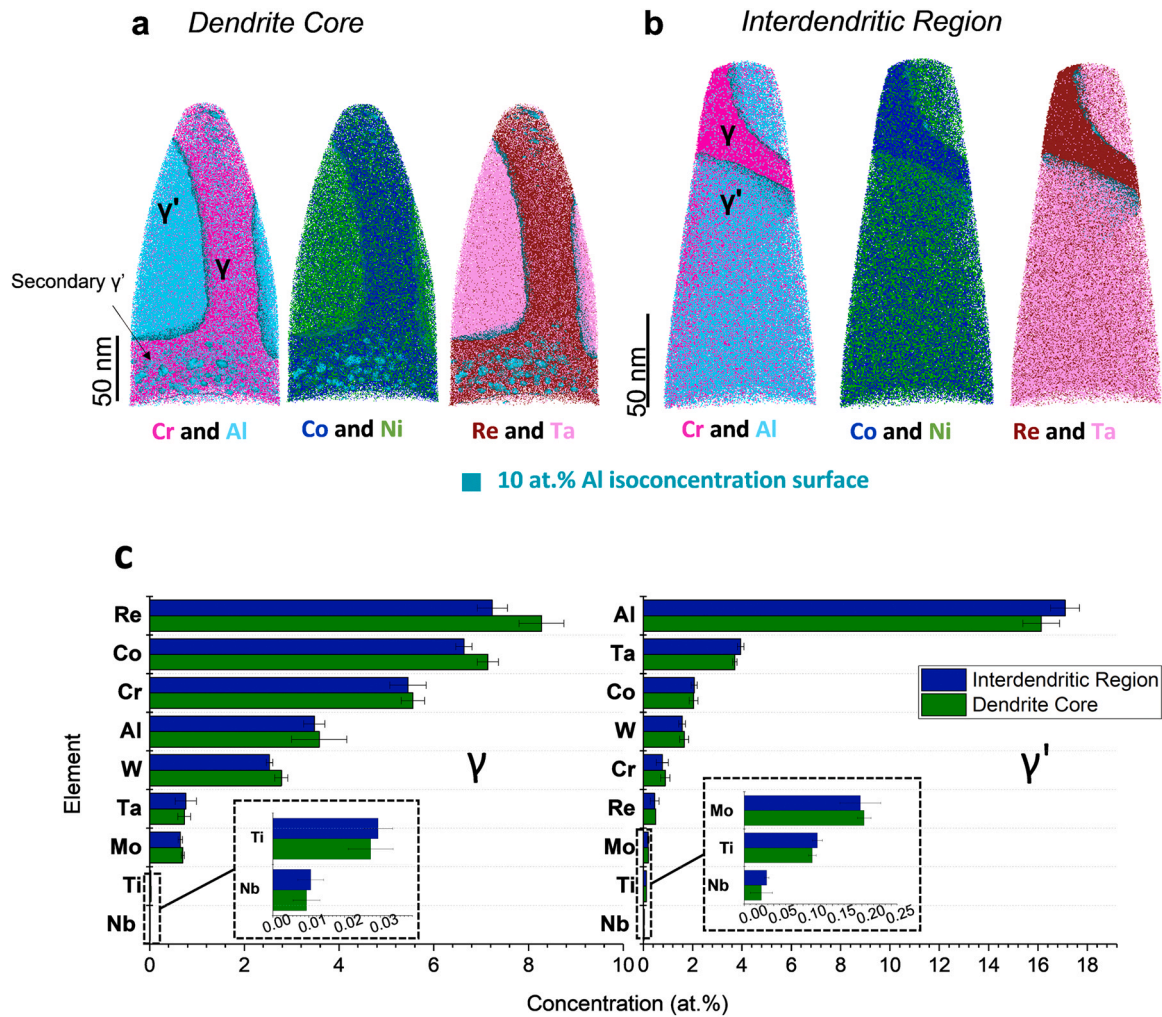
### 3.4. $\gamma/\gamma'$ interfaces

Fig. 8a shows an APT atom map highlighting a cylindrical region of interest (ROI) running through a  $\gamma'$  precipitate, transitioning into a  $\gamma$  channel before entering into another  $\gamma'$  precipitate in a heat-treated dendrite core sample. The corresponding line profile in

Fig. 8b-c shows how the element concentrations vary through the successive phases. It is clear from the profiles there is a substantial depletion of Ni at the interface coupled with an enrichment of Re.

To further understand fluctuations in chemistry at the interface, smaller volumes of atoms containing such interfaces were examined (as demarcated by the dotted line in Fig. 8b-c)) using an Al iso-concentration surface to define the boundary and proximity histograms (proxigrams) to map element behaviour on either side. The average composition across the interface, up to 8 nm away on either side, was analysed relative to the measured bulk concentration of each phase far away from the interface. Only interfaces perpendicular to the specimen axis, where potential data artefacts from field evaporation differences were minimised, were selected for analysis to aid confidence in results.

The resulting proxigrams are shown in Fig. 9, split into as-cast (Fig. 9a) and heat-treated (Fig. 9b), taken from typical DC and IDR in both as-cast and heat-treated conditions, demonstrate the difference in element behaviour across the  $\gamma/\gamma'$  interface between DCs (left) and IDRs (right). Whilst both as-cast and heat-treated samples display an increase in Re on the  $\gamma$  channel side of the interface, matched by a deficit in Ni, the extent of enrichment and depletion was vastly increased within DCs. This interfacial segregation of Re was also higher after heat treatment (Fig. 9b) reaching a peak concentration of 13.2 at% and 10.6 at% in DC and IDR profiles respectively compared to the as-cast condition with a lower peak Re concentration of 12.1 at% in the DC profile and 9.8 at% in the IDR profile (Fig. 9a). At such peaks in the Re content, it was also apparent that the Re profile leading up to the interface was asymmetric, with a steeper gradient noted ahead of the 'bow-wave' shape leading into the  $\gamma'$  phase, compared to a shallower one running into the  $\gamma$  matrix. This phenomenon is likely evidence of Re mobility variation within the two phases. The behaviour of other elements across the interface were more consistent between DCs and IDRs, although slightly higher levels of W on the  $\gamma'$  side of the interface were observed for DCs in both as-cast and heat-treated samples, while Al was noted to deplete on the  $\gamma$  channel side of the interface after heat-treatment in both DCs and



**Fig. 5.** Atom maps from heat-treated RR3010 samples showing Cr, Al, Co, Ni, Re and Ta atoms in (a) dendrite cores and (b) interdendritic regions. (c) composition of  $\gamma$  and  $\gamma'$  phases in heat-treated samples as measured by atom probe.

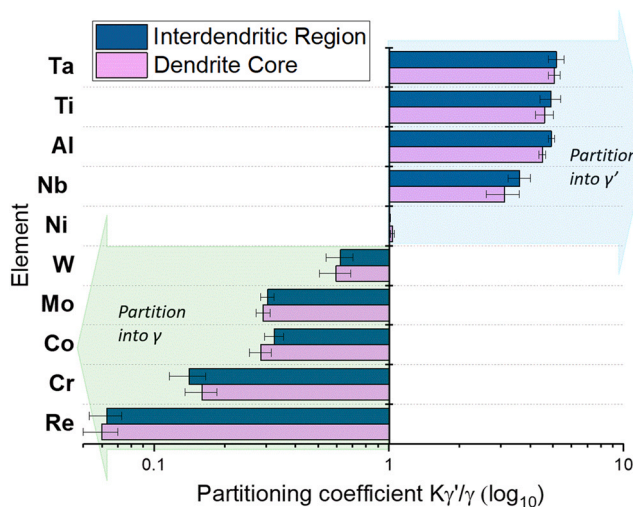


**Fig. 6.** Partitioning ratio of elements into  $\gamma$  and  $\gamma'$  within dendrite cores and interdendritic regions in heat-treated RR3010 samples.

IDRs. Finally, while Re was enriched within the  $\gamma$  channel leading up to the interface, a depletion of Ta on the opposite side of the interface, within the  $\gamma'$ , is also apparent.

## 4. Discussion

### 4.1. Phase chemistry and morphology

The partitioning of elements into DCs and IDRs, as shown in Table 1, highlights the disparity in composition between DCs and IDRs, even after heat treatment. This inhomogeneity across micro-metre length scales is also reflected in compositional and structural differences between  $\gamma$  and  $\gamma'$  phases in these regions. While differences in partitioning behaviour and concentration of each element between DCs and IDRs decreases after heat treatment, a significant difference remains most prominently for Re, Cr and Co in the  $\gamma$  phase and Al and Nb in  $\gamma'$  phase. The element partitioning into  $\gamma$  and  $\gamma'$  phases, as seen in Figs. 3 & 6, showed a strong preference for Re, Mo, Cr, Co and W to partition into  $\gamma$  and Ta, Nb, Ti and Al to partition into  $\gamma'$ . This is in good agreement with the literature and first principle calculations [32,33]. Furthermore, most elements partition more strongly into their preferred phases after heat treatment.

The heat treatment causes  $\gamma'$  precipitates to evolve and grow, along with increasing the extent of partitioning due the faster diffusion kinetics. This is in agreement with experiments and predicted diffusion coefficients of solutes within Ni-alloys [34–36]. Larger increases in partitioning were observed for Ti and Al, both of which are faster diffusing elements within Ni, thus enriching growing  $\gamma'$  at a faster rate compared to Ta and Nb. Of the  $\gamma$  forming elements, Cr displays the biggest change in partitioning extent after heat



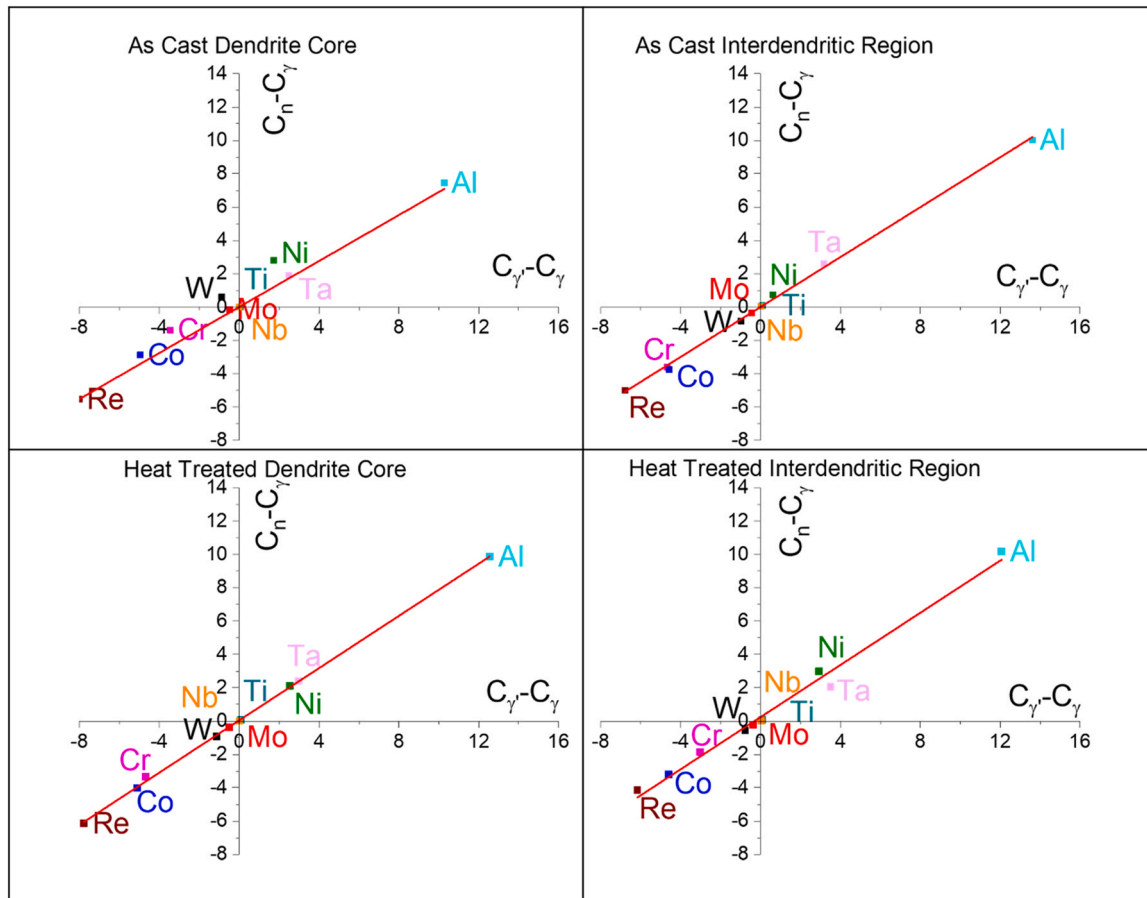


**Fig. 7.** Lever rule plot used for RR3010  $V_f$  calculations in (a) as-cast dendrite core and (b) heat-treated dendrite core (c) as-cast interdendritic region and (d) heat-treated interdendritic region samples.

**Table 2**  
Measured  $V_f$  values calculated using lever rule plots.

Condition	Region	$\gamma'$ $V_f$
As cast	DCs	$0.68 \pm 0.07$
	IDRs	$0.81 \pm 0.08$
Heat-treated	DCs	$0.74 \pm 0.05$
	IDRs	$0.78 \pm 0.04$

treatment, which can similarly be linked to its faster diffusion rate in Ni-X binaries compared to other elements. Conversely, Re and Ta display the smallest change in partitioning into  $\gamma$  and  $\gamma'$  respectively after heat treatment. Both Re and Ta have substantial activation energies for diffusion in Ni and large atomic radii, both of which limit their mobility in the alloy [1,37]. In addition, it has been proposed that strong, directional Ni-Re bonds, unfavourable for solute-vacancy exchanges, decrease the diffusion of Re through Ni [37].

The  $\gamma'$  volume fraction ( $V_f$ ) plays a vital role in dictating the mechanical properties for alloys in high temperature applications, and is consequently an important metric to quantify [5,38]. The  $V_f$  values calculated in Table 2 show a large difference (13%) between DCs and IDRs for the as-cast material, with IDRs having a much higher proportion of  $\gamma'$  precipitates coinciding with increased concentrations of  $\gamma'$  forming elements Al, Ti and Ta. After solutionizing and ageing,  $V_f$  values equalise in both regions, confirming the heat treatment is at least sufficient to prevent mechanical property variations caused by local  $V_f$  fluctuations.

The compositional variation between DCs and IDRs also explains qualitative differences in  $\gamma'$  morphologies and  $V_f$  values observed in the as-cast SEM images (Fig. 1) and APT atom maps (Fig. 2). During

solidification, the liquid is transformed into FCC-gamma, dendrites solidify first, enriched in elements with higher solidification temperatures such as Re and W. As the remaining liquid solidifies, these regions between the dendrites are more heavily concentrated in  $\gamma'$  forming elements such as Al and Ta. Consequently non-equilibrium, large, elongated  $\gamma'$  precipitates form, as shown in Fig. 1d, accommodating the excess  $\gamma'$  forming elements and locally increasing the  $V_f$  within IDRs [39]. In contrast, as-cast DC regions depleted in  $\gamma'$  forming elements were found to have a reduced  $V_f$ . After heat-treatment, elements redistribute via diffusion and the system tends towards an equilibrium phase composition, reducing the local enrichments of  $\gamma'$  forming elements and consequently homogenising  $V_f$  within the different regions. After heat treatment, the  $V_f$  of DC and IDR regions were equivalent within experimental error however EDX and APT showed higher amounts of  $\gamma'$  forming elements were still present within IDR. Many mechanical properties are affected by  $V_f$  and this can have important consequences in the context of IDRs and DCs [40]. For example, the variation in phase chemistry causing changes in  $V_f$  is likely to result in varied mechanical responses between IDRs and DCs. Ensuring solutionizing and ageing times are sufficient for homogenisation is essential in ensuring mechanical properties are homogenous through the alloy.

#### 4.2. Microsegregation

An overall estimation of the composition within DCs and IDRs was obtained by combining all APT compositional measurements from within the respective regions. The partitioning coefficient  $K_i^{DC/IDR} = C_i^{DC}/C_i^{IDR}$  was then determined from these compositions and APT and EDX results compared in Fig. 10. The general behaviour

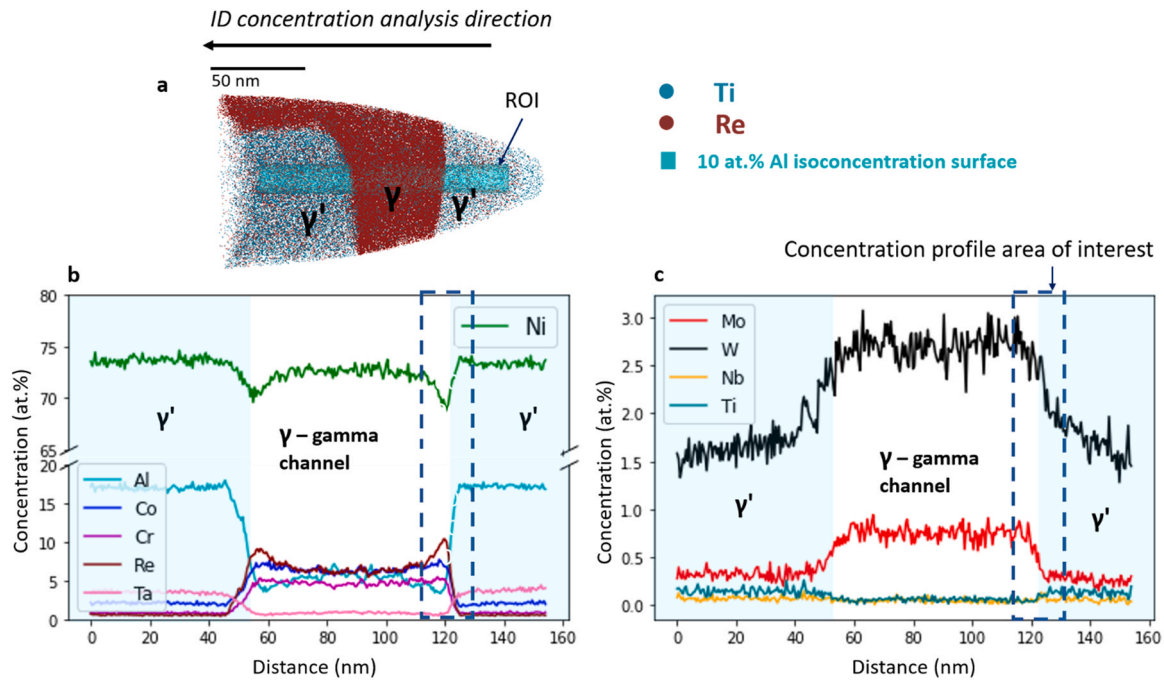


**Fig. 8.** (a) atom map from heat treated DC RR3010 showing Re and Ti atoms with a 10% Al-isoconcentration surface and corresponding 1D concentration profiles along a region of interest (ROI) orientated along the z analysis direction in showing (b) major elements and (c) minor elements.

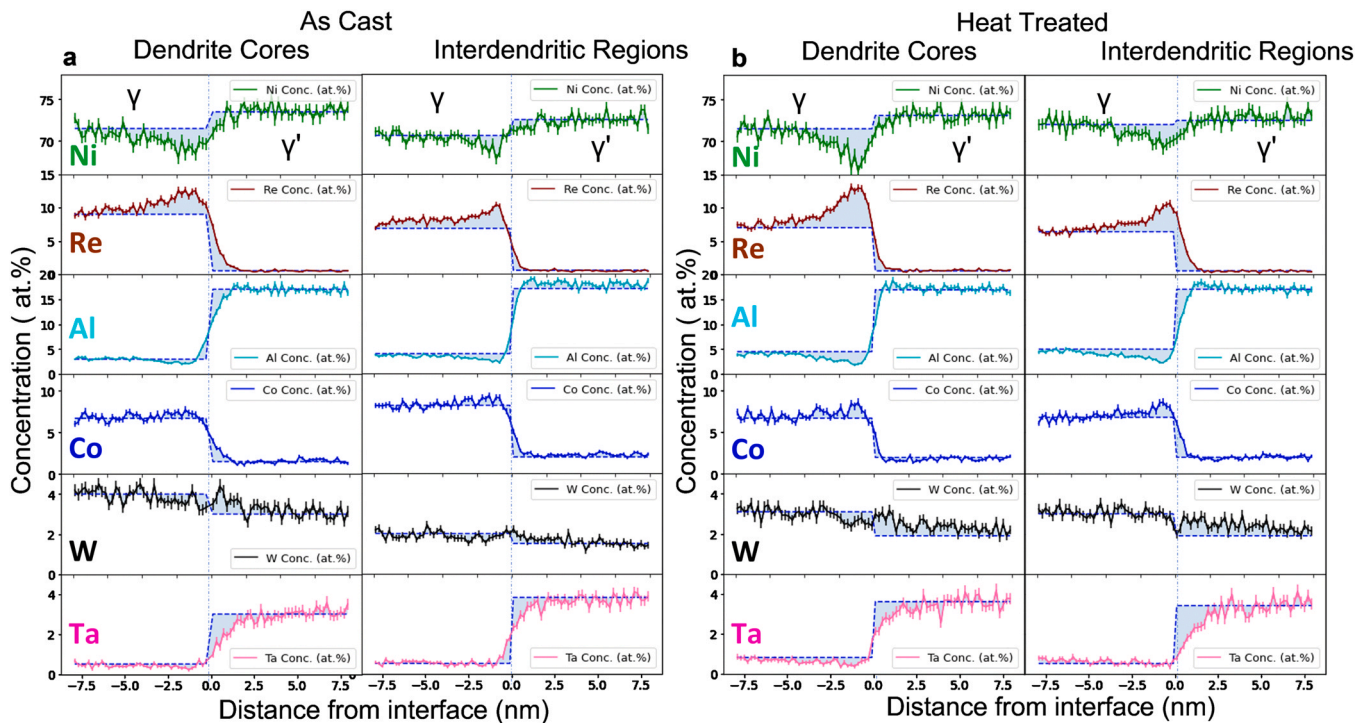


**Fig. 9.** Proxigrams comparing typical measured compositions across  $\gamma/\gamma'$  interfaces to bulk compositions (blue dotted lines) from DC and IDR samples in RR3010 in (a) as cast and (b) heat-treated conditions.

of element partitioning between DCs and IDRs agrees between EDX and APT, with both techniques showing no clear partitioning preference of Ni, while Re, Co, Cr partition into DCs and Al, Ta partition into IDRs before and after heat treatment. These results are consistent with results found within the literature confirming Re, Co, W, Cr enrich within DCs whilst Al and Ta enrich within IDRs [7,8,10,41]. For the partitioning of Re, Cr and Ta, EDX consistently suggested a higher partitioning coefficient compared to APT. The discrepancy in

these results between the two techniques is largely attributed to the increased sensitivity of APT and the lack of impurity detection in EDX.

The techniques also differ over the behaviour of Mo, Ti and Nb. APT results observed Ti and Nb segregating exclusively into IDRs in both as-cast and heat-treated samples, which directly conflicts with the EDX results. This disagreement between techniques is likely due to the detection limits of EDX. As Nb, Ti, and Mo are present in the



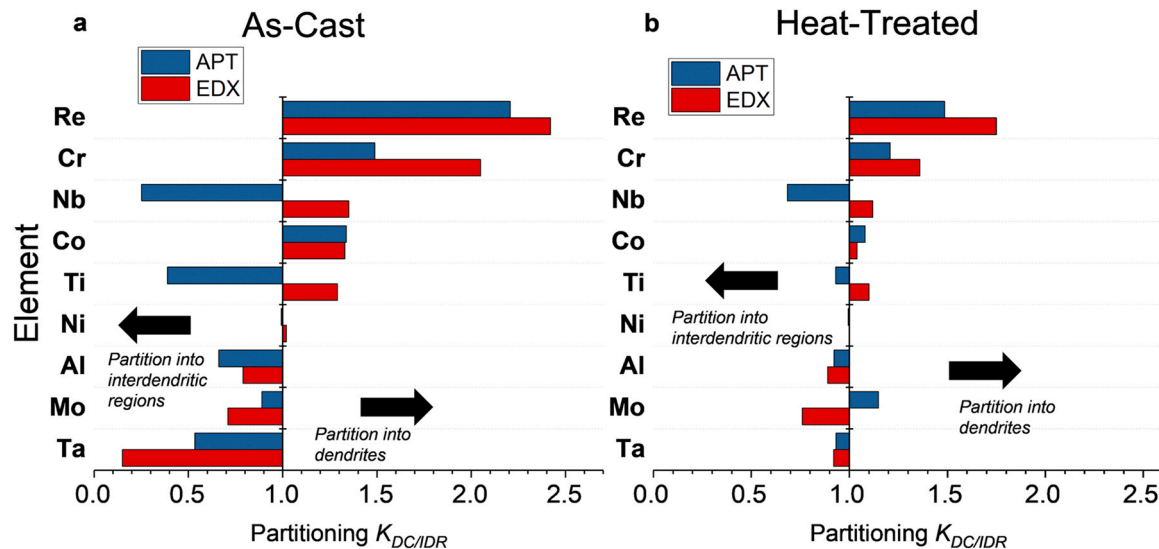


Fig. 10. Plot of dendritic segregation as measured by APT and EDX (a) as-cast and (b) heat-treated samples.

alloy in amounts approaching or below the detection limits of EDX, the enhanced chemical resolution of APT allows for a more accurate quantification of their compositions in regions of the dendrites (and similarly in all other phases). EDX results suggested Mo partitioned into IDRs in both as-cast and heat-treated conditions whilst APT results showed Mo appeared to segregate to IDRs before heat treatment and to DCs after heat treatment. Szcotok and Chmiela showed Mo partitioning into IDRs in the as-cast condition, then partitioning to DCs after a first stage solution heat treatment in CMSX4 [42]. This is in agreement with the results presented in this study. Other studies have also shown other variations in Mo partitioning, with Mo noted to partition into IDRs in some investigations, and DCs in others, all when looking at as-cast materials [13,43]. Overall, these works combined with the current study suggest that the partitioning behaviour of Mo is highly dependent on alloy composition and heat treatment, underlining the need for further dedicated studies. Mo contributes to both solid solution strengthening and corrosion resistance and therefore mapping the behaviour of this element is essential in ensuring the homogenisation and stability across regions [44]. Importantly these results show that some segregation was still evident within the alloy after solutionizing and primary ageing as measured by EDX and APT. This has also been recorded within the literature with the final extent of partitioning heavily influenced by heat treatment specifications [12,13].

#### 4.3. $\gamma/\gamma'$ Interfacial segregation and its effect on lattice parameters and misfit

At the  $\gamma/\gamma'$  interfaces, Re and Ni showed the most striking segregation behaviour with enrichment of Re coupled with depletion of Ni across IDRs and DCs in both as-cast and heat-treated samples. The degree of Re segregation was higher in DCs compared to IDRs and appeared to increase after heat treatment. The Re enrichment occurred within the  $\gamma$  channel side of the interface, suggesting Re is ejected from growing  $\gamma'$  precipitates. The slow mobility of Re within the lattice results in excess atoms aggregating adjacent to the  $\gamma/\gamma'$  interface on the  $\gamma$  channel side [45]. Previous studies have proposed Re diffusion is proportional to the growth of  $\gamma'$  at lower temperatures, but as the temperature increases, the diffusion rate of Re is relatively slower compared to the growth rate of  $\gamma'$  precipitates, causing Re to accumulate at the interface at a greater extent after heat treatment [19,27]. This theory is supported by this study, where

higher Re segregation was observed after heat treatment. It is likely the increased Re segregation at  $\gamma/\gamma'$  interface in DCs compared to IDRs is caused by increased concentrations of Re within DCs, observed before and after heat-treatment by both EDX and APT. Accumulation of Re at an interface has been linked to the formation of a stable dislocation network at  $\gamma/\gamma'$  interfaces, which promotes reduced creep rate [21,46]. This study, where higher levels of Re segregation within DCs was observed, suggests DCs would benefit from increased Re interfacial segregation and consequently may offer better creep properties compared to IDRs. Despite Ni only showing a weak preference for  $\gamma'$  phase over  $\gamma$ , across all samples larger Re excesses were matched by equal depletions of Ni, suggesting Ni is the element accommodating the excess number of Re atoms and plays an important role in stabilizing the interface.

Minor segregations of W to the  $\gamma/\gamma'$  interface were also observed in heat-treated samples which contradicts first principle calculations [23], but is consistent with results found by Sudbrack et al. who also used 3DAP microscopy to investigate interfaces in model Ni-Al-Cr superalloys [47]. Despite W partitioning into  $\gamma$ , along with Re and Co, interfacial enrichment was observed on the  $\gamma'$  precipitate side of the interface. Studies on ternary and multicomponent alloys suggest W preferentially segregates to  $\gamma'$  in the absence of Ta but once Ta is introduced, W is ejected into the  $\gamma$  phase causing a change of W partitioning behaviour [47]. Whilst Ta did not display any obvious interfacial segregation due to the presence of the interface, a very shallow concentration gradient within the  $\gamma'$  precipitate was observed, most pronounced after heat treatment with IDRs. However, another possible cause for the W excess occurring on the  $\gamma'$  side of the interface is excess Re inhibiting W from transitioning across the interface. As the Re builds up at the interface, as seen in Fig. 9, it becomes harder for the W, which has an equally large atomic radius and slow diffusivity, to diffuse across the interface.

There are also several possible explanations for the evolution of this Ta profile. Firstly, it is possible the shape of this profile is indicative of the slow mobility of Ta within the alloy. The slow diffusivity of Ta, results in a decrease in concentration of Ta leading into the interface within the  $\gamma'$ , which enables W to replace Ta and substitute onto the Al-sites within the  $L_{12}$  structure [20]. This theory supports the complementary W profile which shows a slight segregation at the interface on the  $\gamma'$  side of the interface. A second potential cause of the Ta profile is the change in lattice parameter of the  $\gamma$  phase compared to the  $\gamma'$ . As the lattice adopts an altered parameter of the adjacent phase, the constrained lattice is no longer

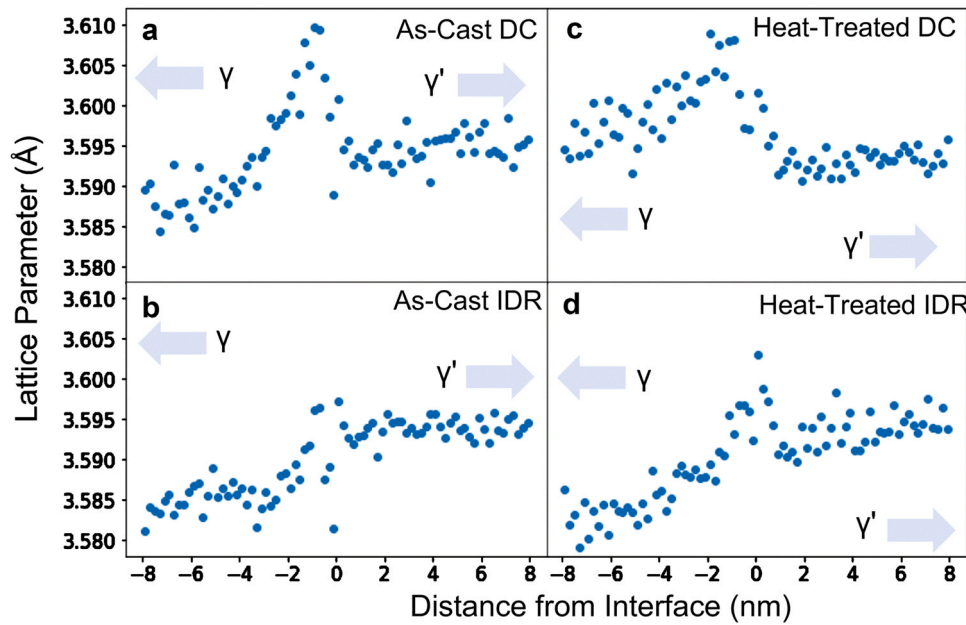


**Fig. 11.** Variation in lattice parameters estimated using Vegard's Law across  $\gamma/\gamma'$  interfaces in as-cast (a) DC and (b) IDR and heat treated (c) DC and (d) IDR regions in RR3010.

able to accommodate the larger atoms such as Ta, which has an 18% difference in atomic diameter from Ni resulting in a 'reduced Ta zone' adjacent to the interface in a similar mechanism to that proposed by Bagot et al. to explain the reduction of Hf adjacent to  $\gamma'/\gamma$  interface within polycrystalline RR1000 [25]. More likely, the observed decrease of Ta adjacent to the  $\gamma'/\gamma$  interface is a combination of both these kinetic and size effects causing the resulting profile shape but it is unclear from these profiles which is the dominant effect and further work is needed to understand the evolution of the element profiles with both heat treatment and compositional changes.

In addition to how elements may influence the concentration at the interface, how elements affect the lattice parameter and in turn may be influenced by the lattice parameter are key factors when considering alloying additions, particularly the effect that each element has on the lattice misfit [1]. Lattice misfit is defined as  $= 2 \left( \frac{a_{\gamma'} - a_{\gamma}}{a_{\gamma'} + a_{\gamma}} \right)$ , where  $a_{\gamma'}$  and  $a_{\gamma}$  are the lattice parameters of  $\gamma'$  and  $\gamma$  phases respectively. Lattice parameters,  $a_{\gamma'}$  and  $a_{\gamma}$  can be predicted by use of Vegard's Law:  $a_{\gamma'} = a_0^{\gamma'} + \sum_i \Gamma_i^{\gamma'} x_i^{\gamma'}$ ,  $a_{\gamma} = a_0^{\gamma} + \sum_i \Gamma_i^{\gamma} x_i^{\gamma}$  where  $a_0^{\gamma'}$  and  $a_0^{\gamma}$  are the lattice parameters of pure Ni and Ni<sub>3</sub>Al,  $\Gamma_i^{\gamma'}$  and  $\Gamma_i^{\gamma}$  are the Vegard's coefficients of element  $i$  in  $\gamma'$  and  $\gamma$  phases and  $x_i^{\gamma'}$  and  $x_i^{\gamma}$  are the mole fractions of element  $i$  in  $\gamma'$  and  $\gamma$  respectively. As a consequence of this equation, lattice parameter scales linearly with composition. If local enrichments or depletions occur adjacent to an interface, affecting local concentrations, the local lattice parameter next to the interface can be expected to fluctuate, which could lead to changes in local lattice misfit. As an example, using Vegard's law, the lattice parameters leading up to and away from the interface from the profiles observed in Fig. 9 were calculated and shown in Fig. 11.

Fig. 11 clearly demonstrates the strong dependency between lattice parameter and local fluctuations in chemistry. In all cases, the lattice parameter was more strongly dependent on local compositions within the  $\gamma$  phase, where large fluctuations were present and an increase in  $\gamma$  lattice parameter with decreasing distance to the interface was noted. By comparison, lattice parameters within  $\gamma'$  phases appeared to be more consistent with a roughly constant lattice parameter estimated across the  $\gamma'$  phase leading away from the interface. A positive lattice misfit, defined by  $a_{\gamma'} > a_{\gamma}$ , was suggested in all samples apart from heat-treated DC samples which

suggested a negative lattice misfit and  $a_{\gamma'} < a_{\gamma}$ . These results are in agreement with those found by Bruckner et al. who investigated the effect of dendritic structures in a third generation superalloy and found similar trends in lattice parameters between DCs and IDRs as measured by x-ray diffraction [41]. The sign of the misfit plays an important role in determining the stress state of the material with conflicting opinions within the literature as to whether a positive or negative misfit is overall more preferable and further work is clearly needed to understand the potential variation in misfit sign with region within these alloys [21,48–50]. Interestingly these results suggest a larger lattice misfit is observed within IDR, despite overall larger lattice parameters observed in DC. The high dependency between composition and local lattice parameter as observed in this study may help to explain conflicting mechanical responses between DCs and IDRs reported in the literature [14,15] where three different single crystal Ni-based superalloys with varying concentrations of alloying elements were investigated.

Composition fluctuations between DCs and IDRs, such as higher Re concentrations associated with DCs, which resulted in higher segregation of Re at the  $\gamma/\gamma'$  interface, can consequently have a significant effect on mechanical properties between the two regions by altering the local lattice parameters of each phase and the overall lattice misfit. Whilst it is impractical to absolutely quantify an interfacial width from APT data, the comparison of elements across conditions is possible and these results clearly demonstrate the disparity between DCs and IDRs. With most notable differences in Re and Ni between DCs and IDRs, it is important to understand how these elements behave across the interface. Furthermore, the change in concentration across the interface highlights a region within the alloy that is deviated from the expected compositions and could affect other properties, such as corrosion resistance. Further work is needed to understand interface evolution across conditions and their influential roles in dictating potential local changes in mechanical and physical properties between DCs and IDRs.

## 5. Conclusions

These results clearly show that even minimal residual segregation between dendrites and surrounding interdendritic regions influences the local concentrations of  $\gamma$  and  $\gamma'$  phases in a single crystal



Ni-superalloy, and furthermore has a profound effect on element phase partitioning and interfacial behaviour.

- Clear chemical variation was observed between DCs and IDRs even after a heat treatment, particularly for elements Re, Cr, Nb and Ta.
- The inhomogeneity of chemistry and microstructure shown in these results is due to segregation of elements into DCs and IDRs, highlights the importance of site-specific analysis by APT.
- Good agreement is seen between partitioning coefficients between EDX and APT, but the greater chemical resolution of APT additionally shows that Ti and Nb partition into IDRs, whilst Mo changes its partitioning preference depending on heat treatment.
- Fluctuations in local  $\gamma$  and  $\gamma'$  chemistry driven by microsegregation were shown to cause changes in lattice parameter and misfit within DCs and IDRs.
- Increased interfacial Re segregation along with similar other elemental variations within DCs compared to IDRs could have important implications in understanding mechanical property differences between the two regions.

These results clearly highlight the importance for complete heat treatments of these alloys to obtain full homogeneity and consistent elemental and mechanical behaviour across the alloy, and that site-specific use of APT to verify any residual inhomogeneity can offer unique insights into understanding in-service performance of these materials.

#### CRedit authorship contribution statement

**V.C.I. Strutt:** Conceptualization, Methodology, Visualization, Writing – original draft, Writing – review & editing. **B.M. Jenkins:** Writing – review & editing. **J.M. Woolrich:** Writing – review & editing, Resources. **M. Appleton:** Writing – review & editing, Resources. **M.P. Moody:** Writing – review & editing, Supervision. **P.A.J. Bagot:** Writing – review & editing, Supervision.

#### Data availability

The data that has been used is confidential.

#### Declaration of Competing Interest

The authors declare that they have no known competing financial interests or personal relationships that could have appeared to influence the work reported in this paper.

#### Acknowledgment

This research was sponsored by Rolls-Royce plc and the Oxford Atom probe facility was funded by EPSRC (EP/M022803/1).

#### References

- [1] R.C. Reed, *The Superalloys: Fundamentals and Applications*, Cambridge University Press, Cambridge, 2006.
- [2] S. Tin, L. Zhang, R.A. Hobbs, A.C. Yeh, C.M.F. Rae, and B. Broomfield, Linking the properties, processing and chemistry of advanced single crystal ni-base superalloys, in *Proceedings of the International Symposium on Superalloys*, 2008, pp. 81–90.
- [3] A. Heckl, S. Neumeier, M. Göken, R.F. Singer, The effect of Re and Ru on  $\gamma/\gamma'$  microstructure,  $\gamma$ -solid solution strengthening and creep strength in nickel-base superalloys, *Mater. Sci. Eng. A* vol. 528, (9) (2011) 3435–3444.
- [4] N. D'Souza, W. Li, C. Argyrakos, G.D. West, C.D. Slater, On the Evolution of Primary Gamma Prime Precipitates During High Temperature and High Strain Rate Deformation and Subsequent Heat Treatment in the Ni-Based Superalloy, RR1000, *Metall. Mater. Trans. A Phys. Metall. Mater. Sci.* vol. 50, (9) (2019) 4205–4222.
- [5] D. Mukherji, J. Rösler, Effect of the  $\gamma'$  volume fraction on the creep strength of Ni-base superalloys, *Z. fuer Met. Res. Adv. Tech.* vol. 94, (5) (2003) 478–484.
- [6] G.N. Maniar, J.E. Bridge, Effect of gamma-gamma prime mismatch, volume fraction gamma prime, and gamma prime morphology on elevated temperature properties of Ni, 20 Cr, 5.5 Mo, Ti, Al alloys, *Metall. Trans.* vol. 2, (1) (. 1971) 95–102.
- [7] R.A. Hobbs, S. Tin, C.M.F. Rae, R.W. Broomfield, and C.J. Humphreys, "Solidification characteristics of advanced nickel-base single crystal superalloys," in *Proceedings of the International Symposium on Superalloys*, 2004, pp. 819–825.
- [8] H.T. Pang, N. D'Souza, H. Dong, H.J. Stone, C.M.F. Rae, Detailed Analysis of the Solution Heat Treatment of a Third-Generation Single-Crystal Nickel-Based Superalloy CMSX-10K\*, *Metall. Mater. Trans. A* vol. 47, (2) (2016) 889–906.
- [9] R.A. Hobbs, S. Tin, C.M.F. Rae, A castability model based on elemental solid-liquid partitioning in advanced nickel-base single-crystal superalloys, *Metall. Mater. Trans. A Phys. Metall. Mater. Sci.* vol. 36, (10) (2005) 2761–2773.
- [10] H.T. Pang, H.J. Stone, C.M.F. Rae, L. Zhang, R.A. Hobbs, Solution heat treatment optimization of fourth-generation single-crystal nickel-base superalloys, *Metall. Mater. Trans. A Phys. Metall. Mater. Sci.* vol. 43, (9) (2012) 3264–3282.
- [11] R.M. Kearsey, J.C. Beddoes, K.M. Jaansalu, W.T. Thompson, and P. Au, "The effects of Re, W and Ru on microsegregation behaviour in single crystal superalloy systems," in *Proceedings of the International Symposium on Superalloys*, 2004, pp. 801–810.
- [12] L. Zhang, Z. Huang, L. Jiang, J. Luan, Z. Jiao, C.T. Liu, Effect of Mo:W ratio on segregation behavior and creep strength of nickel-based single crystal superalloys, *Mater. Sci. Eng. A* vol. 744, (2019) 481–489.
- [13] A. Paraschiv, G. Matache, C. Puscasu, The effect of heat treatment on the homogenization of CMSX-4 Single-Crystal Ni-Based Superalloy, *Transp. Res. Procedia* vol. 29, (2017) (2018) 303–311.
- [14] C. Tromas, M. Arnoux, X. Milhet, Hardness cartography to increase the nanoindentation resolution in heterogeneous materials: Application to a Ni-based single-crystal superalloy, *Scr. Mater.* vol. 66, (2) (2012) 77–80.
- [15] G.X. Lu, J.D. Liu, Y.Z. Zhou, T. Jin, X.F. Sun, Z.Q. Hu, Differences in the micro-mechanical properties of dendrites and interdendritic regions in superalloys, *Philos. Mag. Lett.* vol. 96, (12) (2016) 461–468.
- [16] A.B. Parsa, et al., Advanced scale bridging microstructure analysis of single crystal Ni-base superalloys, *Adv. Eng. Mater.* vol. 17, (2) (2015) 216–230.
- [17] D. Ma, U. Gfarte, Microsegregation in directionally solidified dendritic-cellular structure of superalloy CMSX-4, *Mater. Sci. Eng. A* vol. 270, (2) (1999) 339–342.
- [18] H.T. Pang, et al., Microstructure and solidification sequence of the interdendritic region in a third generation single-crystal nickel-base superalloy, *Metall. Mater. Trans. A Phys. Metall. Mater. Sci.* vol. 40, (7) (2009) 1660–1669.
- [19] J. Zhang, et al., Unveiling the Re segregation at  $\gamma/\gamma'$  interface in Ni-based superalloy, *Scr. Mater.* vol. 204, (2021) 114131.
- [20] F. Lu, et al., Unveiling the Re effect on long-term coarsening behaviors of  $\gamma'$  precipitates in Ni-based single crystal superalloys, *Acta Mater.* vol. 233, (2022) 117979.
- [21] A.R. Khoei, M. Youzi, G.T. Eshlaghi, Mechanical properties and  $\gamma/\gamma'$  interfacial misfit network evolution: A study towards the creep behavior of Ni-based single crystal sup. *Mech. Mater.* vol. 171, (May) (2022) 104368.
- [22] A. Mottura, R.C. Reed, What is the role of rhenium in single crystal superalloys? *MATEC Web Conf.* vol. 14, (2014) 1–6.
- [23] Y. Amouyal, Z. Mao, D.N. Seidman, Segregation of tungsten at  $\gamma'$  (L 12) /  $\gamma$  (fcc) interfaces in a Ni-based superalloy: An atom-probe tomographic and first-principles study, *Appl. Phys. Lett.* vol. 93, (20) (2008) 1–4.
- [24] P.J. Warren, A. Cerezo, G.D.W. Smith, An atom probe study of the distribution of rhenium in a nickel-based superalloy, *Mater. Sci. Eng. A* vol. 250, (1) (1998) 88–92.
- [25] P.A.J. Bagot, et al., An Atom Probe Tomography study of site preference and partitioning in a nickel-based superalloy, *Acta Mater.* vol. 125, (2017) 156–165.
- [26] Y. Amouyal, Z. Mao, D.N. Seidman, Phase partitioning and site-preference of hafnium in the  $\gamma'$  (L 12) /  $\gamma$  (fcc) system in Ni-based superalloys: An atom-probe tomographic and first-principles study, *Appl. Phys. Lett.* vol. 95, (16) (2009).
- [27] W. Yang, et al., The Element Segregation Between  $\gamma/\gamma'$  Phases in a Ni-Based Single Crystal Superalloy Studied by 3D-APT and Its Potential Impact on Local Interfacial Misfit Strain, *Met. Mater. Int.* vol. 27, (6) (2021) 1892–1896.
- [28] B. Gault, M.P. Moody, J.M. Cairney, S.P. Ringer, *Atom Probe Microscopy* vol. 160, Springer, New York, NY, 2012.
- [29] M.K. Miller, K.F. Russell, K. Thompson, R. Alvis, D.J. Larson, Review of Atom Probe FIB-Based Specimen Preparation Methods, *Microsc. Microanal.* vol. 13, (6) (2007) 428–436.
- [30] A.J. London, Quantifying Uncertainty from Mass-Peak Overlaps in Atom Probe Microscopy, *Microsc. Microanal.* vol. 25, (2) (2019) 378–388.
- [31] T. Homma, A. Arafah, D. Haley, M. Nakai, M. Niinomi, M.P. Moody, Effect of alloying elements on microstructural evolution in oxygen content controlled Ti-29Nb-13Ta-4.6Zr (wt%) alloys for biomedical applications during aging, *Mater. Sci. Eng. A* vol. 709, (July 2017) (2018) 312–321.
- [32] N. Wanderka, U. Glatzel, Chemical composition measurements of a nickel-base superalloy by atom probe field ion microscopy, *Mater. Sci. Eng. A* vol. 203, (1–2) (1995) 69–74.
- [33] M. Chaudhari, et al., Site occupancy of chromium in the  $\gamma'$ -Ni 3Al phase of nickel-based superalloys: A combined 3D atom probe and first-principles study, *Philos. Mag. Lett.* vol. 92, (9) (2012) 495–506.
- [34] M. Kolb, et al., Influence of rhenium on  $\gamma'$ -strengthened cobalt-base superalloys, *J. Mater. Res.* vol. 32, (13) (2017) 2551–2559.

- [35] W. Qiong, L. Shu-Suo, M. Yue, G. Sheng-Kai, First principles calculations of alloying element diffusion coefficients in Ni using the five-frequency model, *Chin. Phys. B* vol. 21, (2012) 109102.
- [36] C. SUDBRACK, K. YOON, R. NOEBE, D. SEIDMAN, Temporal evolution of the nanostructure and phase compositions in a model Ni–Al–Cr alloy, *Acta Mater.* vol. 54, (12) (2006) 3199–3210.
- [37] C.L. Fu, R. Reed, A. Janotti, and M. Kremer, "On the Diffusion of Alloying Elements in the Nickel-Base Superalloys," in *Superalloys 2004 (Tenth International Symposium)*, 2004, no. June 2014, pp. 867–876.
- [38] M.A. Ali, et al., Effect of  $\gamma'$  precipitate size on hardness and creep properties of Ni-base single crystal superalloys: Experiment and simulation, *Materialia* vol. 12, (2020).
- [39] K. Park, P. Withey, Compositions of Gamma and Gamma Prime Phases in an As-Cast Nickel-Based Single Crystal Superalloy Turbine Blade, *Crystals* vol. 12, (2) (2022) 299.
- [40] T. Murakumo, Y. Koizumi, K. Kobayashi, H. Harada, Creep strength of Ni-base single-crystal superalloys on the  $\gamma/\gamma'$  tie-line, *Proc. Int. Symp. Superalloys (2004)* 155–162.
- [41] U. Brückner, A. Epishin, T. Link, K. Dressel, The influence of the dendritic structure on the  $\gamma/\gamma'$ -lattice misfit in the single-crystal nickel-base superalloy CMSX-4, *Mater. Sci. Eng. A* vol. 247, (1–2) (1998) 23–31.
- [42] A. Szczotok, B. Chmiela, Effect of heat treatment on chemical segregation in CMSX-4 nickel-base superalloy, *J. Mater. Eng. Perform.* vol. 23, (8) (2014) 2739–2747.
- [43] G. Matache, D.M. Stefanescu, C. Puscasu, E. Alexandrescu, Dendritic segregation and arm spacing in directionally solidified CMSX-4 superalloy, *Int. J. Cast. Met. Res.* vol. 29, (5) (2016) 303–316.
- [44] S.J. Park, S.M. Seo, Y.S. Yoo, H.W. Jeong, H.J. Jang, Effects of Cr, W, and Mo on the high temperature oxidation of Ni-based superalloys, *Mater. (Basel)*. vol. 12, (18) (2019).
- [45] A. Mottura, N. Warnken, M.K. Miller, M.W. Finnis, R.C. Reed, Atom probe tomography analysis of the distribution of rhenium in nickel alloys, *Acta Mater.* vol. 58, (3) (2010) 931–942.
- [46] X. Wu, et al., Unveiling the Re effect in Ni-based single crystal superalloys, *Nat. Commun.* vol. 11, (1) (2020) 389.
- [47] C.K. Sudbrack, D. Isheim, R.D. Noebe, N.S. Jacobson, D.N. Seidman, The Influence of Tungsten on the Chemical Composition of a Temporally Evolving Nanostructure of a Model Ni–Al–Cr Superalloy, *Microsc. Microanal.* vol. 10, (3) (2004) 355–365.
- [48] K. Arora, K. Kishida, K. Tanaka, H. Inui, Effects of lattice misfit on plastic deformation behavior of single-crystalline micropillars of Ni-based superalloys, *Acta Mater.* vol. 138, (2017) 119–130.
- [49] H. Mughrabi, The importance of sign and magnitude of  $\gamma/\gamma'$  lattice misfit in superalloys - With special reference to the new  $\gamma'$ -hardened cobalt-base superalloys, *Acta Mater.* vol. 81, (2014) 21–29.
- [50] J.X. Zhang, J.C. Wang, H. Harada, Y. Koizumi, The effect of lattice misfit on the dislocation motion in superalloys during high-temperature low-stress creep, *Acta Mater.* vol. 53, (17) (2005) 4623–4633.